https://doi.org/10.48048/tis.2023.7021

Morphological Evolution of TiO_2 Nanoparticle Deposited on QCM Sensor at Various Calcination Temperature

Dhafi Alvian Nugraha[1], Safira Rachmaniar[1], Rachmat T. Tjahjanto[2], Setyawan P. Sakti[1], Dionysius J. D. H. Santjojo[1] and Masruroh[1,*]

[1]Physics Department, Faculty of Mathematics and Natural Sciences, Brawijaya University, Indonesia
[2]Chemistry Department, Faculty of Mathematics and Natural Sciences, Brawijaya University, Indonesia

([*]Corresponding author's e-mail: ruroh@ub.ac.id)

Received: 26 April 2023, Revised: 29 May 2023, Accepted: 30 May 2023, Published: 28 August 2023

Abstract

The morphology of TiO_2 nanoparticles deposited on a QCM sensor is crucial in its mechanical loading. Different heating treatments transform the morphology of TiO_2 nanoparticles, affecting the loading and hence shifting the resonant frequency and changing the impedance QCM value. In this research, the deposition of TiO_2 nanoparticles was carried out above QCM using the ultrasonic spray pyrolysis (USP) technique with variations in calcination temperature of 200, 230, and 250 °C. The analysis results show that the increase in the agglomeration and particle size causes an increase in the inertial mass of TiO_2 nanoparticles.

Keywords: TiO_2 nanoparticle, Ultrasonic spray pyrolysis, Calcination temperature, QCM sensor, Impedance analysis

Introduction

TiO_2 is an n-type metal oxide material with a wide band gap. TiO_2 nanomaterials are widely applied as photocatalysts [1-4], gas sensors [5-8], and solar cells [9]. The most common reasons for using these materials are because they have chemical stability, are environmentally inert, and are relatively inexpensive to synthesize. The crystalline phase structure of TiO_2 has 3 main types of polymorphs; brookite, anatase, and rutile. The anatase phase is more suitable for gas sensor material because it has a larger band gap energy, wider surface area, and strong oxidizing power. It is also stable against photo-corrosion and has more efficient electron transport than other types of TiO_2 [10,11]. TiO_2 was chosen as the sensor material because it has a lot of oxygen vacancies, high surface area morphology, high reactivity, and selectivity for CO, which is present in many hydrocarbon gases [7].

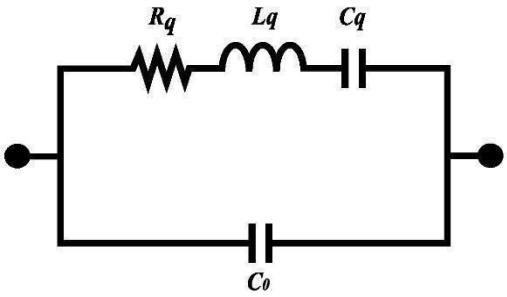

Figure 1 Butterworth-van Dyke (BVD) circuit model of QCM sensor.

Quartz crystal microbalance (QCM) acoustic sensors can be found in many applications. The benefit of using the QCM is that it is robust, inexpensive, accurate, and highly sensitive to measure mass changes in nanograms/cm^2 to micrograms/cm^2 [12]. The sensor's performance is characterized by its sensitivity and selectivity. It can be improved by modifying the morphology of the sensor's surface and adding a nano- or micro-structured layer on the surface [13]. The nanostructured layer increases the sensor's sensitivity because the exposed surface area with the analyte is larger [11]. The additional nano- or micro-structured

layers increase the load mass, which will affect the mechanical oscillation of the QCM acoustic sensor. The loading behavior can be predicted by modeling the system in an electrical equivalent circuit [14].

The QCM system is usually modeled using the Butterworth-van Dyke (BVD) equivalent circuit (**Figure 1**). The BVD circuit consists of a motional arm and a static arm. The capacitor (C_0) on the static arm represents the capacitance value of the electrode with the crystal as the dielectric material. While the motional arm has a series of R_q, L_q, and C_q. Resistor (R_q) represents the damping value per oscillation, Inductor (L_q) is an inertial element that is equivalent to the mass of the crystal, and capacitor (C_q) represents the stored energy value per oscillation and is inversely proportional to the crystal stiffness [15,16]. The oscillation frequency of the sensor depends on the thickness or mass of the layer deposited above the sensor. It affects the value of the components in the BVD equivalent circuit [14]. Researchers show that the addition of layers on the QCM can be modeled by incorporating relevant components in the BVD equivalent circuit [17,18]. The modified BVD circuit can also accurately clarify the effect of extra layers on the resonance frequency [19,20].

The synthesis of TiO_2 nanoparticles can be carried out in several methods, such as sol-gel [21], sputtering [22], plasma-enhanced chemical vapor deposition (PECVD) [23], a spin-coating process [24], laser ablation [25], and ultrasonic spray pyrolysis [26]. Based on these methods, ultrasonic spray pyrolysis is one of the attractive methods for producing TiO_2 nanoparticles because the resulting powder has a round and porous shape so that the surface is smooth. The technique has different procedures and stages to produce different microstructures and morphology. The optimized morphology of the powder surface creates a more extensive interaction between the particles and analyte [1]. In addition, this method has many advantages, such as low costs, continuous operation, high rates of synthesis and deposition, and no need for a vacuum to operate [27]. Parameters affecting the particle formation process can be controlled based on the calcination temperature, carrier gas flow rate, precursor used, time, and frequency of the ultrasonic nebulizer used [1,27,28].

There are limited studies on synthesizing TiO_2 nanoparticles on top of QCM. The limitation is that the QCM sensor device is susceptible to calcination treatment. This research will focus on synthesizing TiO_2 nanoparticles deposited on top of the QCM in a series of processes using the ultrasonic spray pyrolysis method on top of the QCM with varied calcination temperatures. The purpose of this research is to be able to synthesize TiO_2 nanoparticles deposited on top of the QCM without damaging the sensor device. Additionally, the relation among the calcination temperature, morphological evolution, and resonance frequency will be analyzed.

Materials and methods

Synthesis and deposition of TiO_2 nanoparticle

Precursor preparation begins by mixing titanium tetra isopropoxide ($Ti(OCH(CH_3)_2)_4$) with C_2H_6O ethanol to obtain a solution with a concentration of 0.5 M. Then the answer is stirred with a magnetic stirrer for 30 min at 500 rpm to obtain a homogeneous precursor solution.

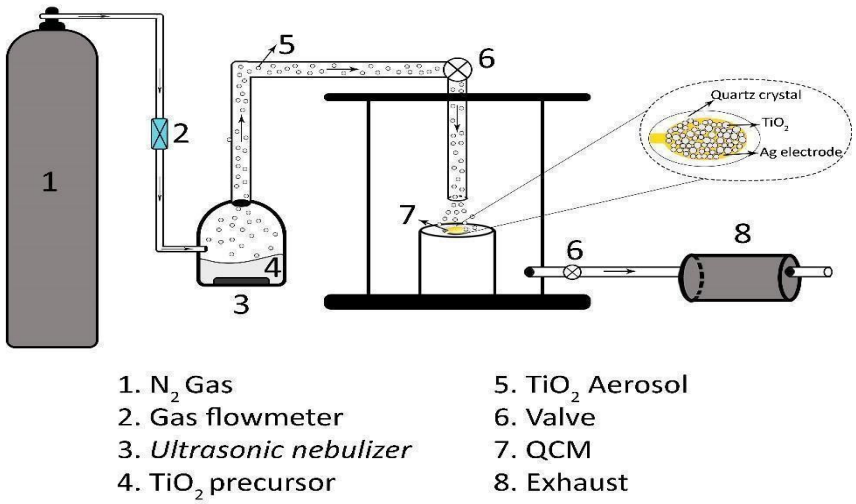

Figure 2 Ultrasonic spray pyrolysis system.

The ultrasonic spray system is shown in **Figure 2**. The homogeneous solution is then transferred to a container. The first step is to turn on the ultrasonic nebulizer with a frequency of 108 kHz and open the nitrogen gas valve as the carrier gas. The ultrasonic nebulizer will produce an aerosol, which will be carried by nitrogen gas as a carrier gas. The carrier gas flow rate was kept constant at 75 mL/min. This stage is carried out for 30 min. In the second stage, the deposited TiO_2 nanoparticles were heated using an oven at 100 °C for 1 h. Next, the TiO_2 sample is calcined. The TiO_2 sample without the addition of calcination was carried out as a comparison. For other samples, the calcination was continued at 200, 230, and 250 °C for 2 h, followed by natural cooling overnight.

Characterization and impedance measurement

The morphology of the shape and size of TiO_2 nanoparticles were observed with a field emission scanning electron microscope (FESEM) type Quanta FEG 650 FEI. Then, changes in the impedance of the QCM sensor before and after coating TiO_2 nanoparticles were measured with the impedance analyzer Bode 100, OMICRON Electronics Asia Ltd., Hongkong. In the setup shown in **Figure 3**, the analyzer was connected to a computer, and their results were imaginary and real impedance values, frequency, and phase differences.

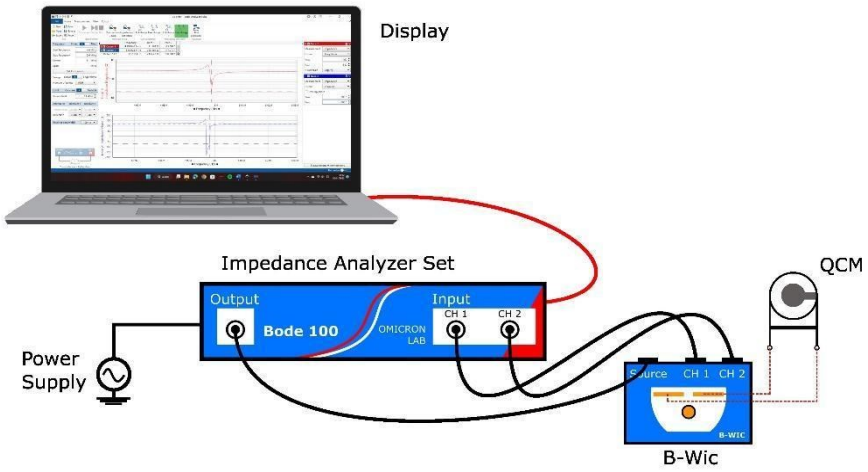

Figure 3 Setup for impedance measurement using impedance analyzer Bode 100, OMICRON LAB.

Results and discussion

Result

TiO_2 morphology and size with variations in calcination temperature are shown in **Figure 4**. The calcination temperature significantly affects the nanostructures of the particles formed. The figure shows that the particle size of TiO_2 increases with increasing calcination temperature. TiO_2 nanoparticles without calcination (**Figure 4(a)**), calcination at 200 °C (**Figure 4(b)**), and 230 °C (**Figure 4(c)**) appear to have a spherical shape. TiO_2 nanoparticles without calcination have small particle sizes (**Figure 4(a)**). At a calcination temperature of 200 °C, the nanoparticles were seen to be separated with relatively homogeneous particle size (**Figure 4(b)**). At the calcination temperature of 230 °C, the formed nanoparticles were not homogeneous in size (**Figure 4(c)**). Significant changes occur when the calcination temperature is increased to 250 °C. The particles are seen to diffuse to form agglomerations between particles (**Figure 4(d)**). Particles originally formed individually become joined to form a chain of agglomerated nanoparticles. The higher the calcination temperature, the particle size homogeneity decreases.

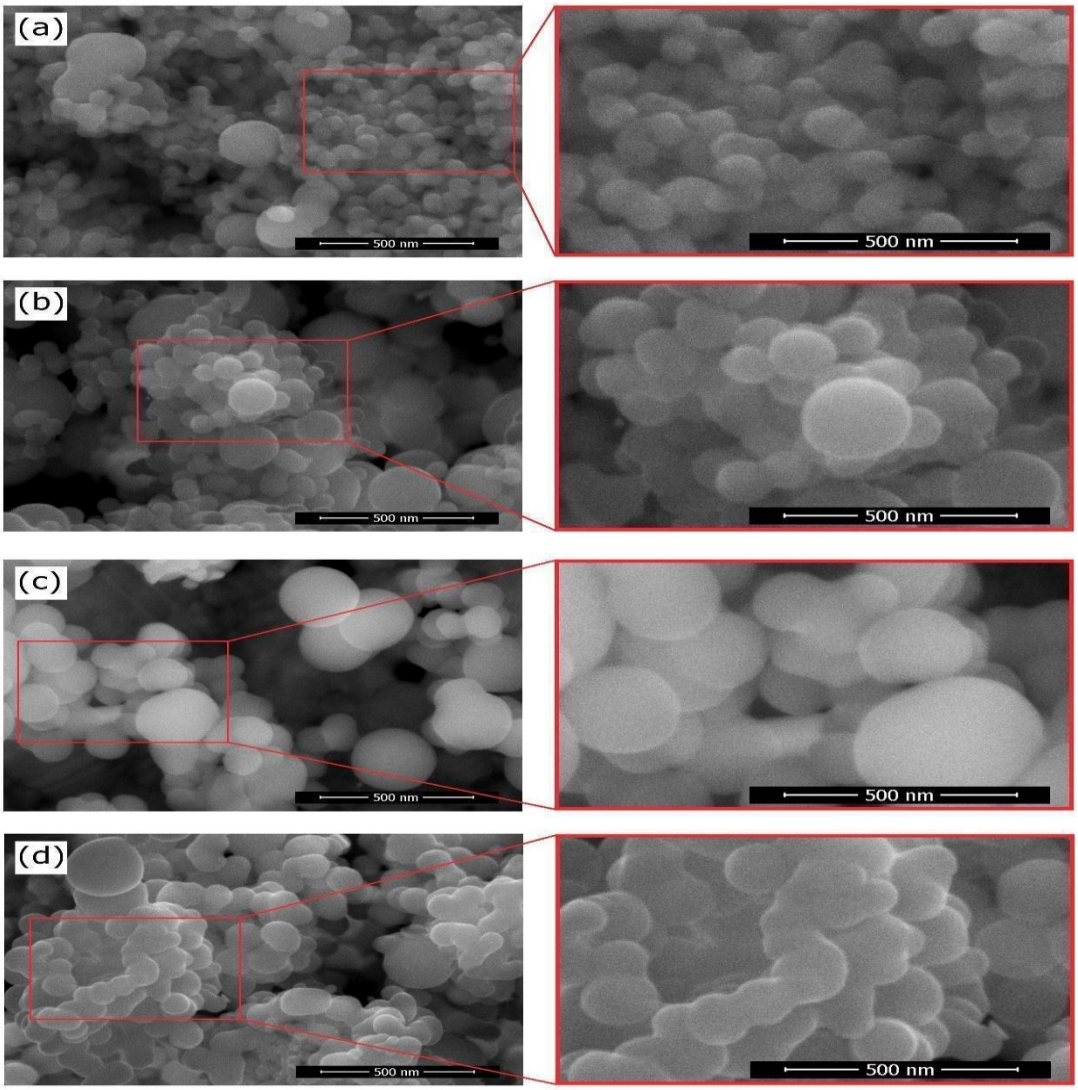

Figure 4 SEM images of TiO_2 nanoparticles with variations in calcination temperature (a) uncalcined, (b) 200 °C, (c) 230 °C, and (d) 250 °C.

Increasing the calcination temperature in the synthesis of TiO_2 nanoparticles using the sol-gel method [29] and USP [30], increased the size of TiO_2 nanoparticles. In this research, particle size distribution with variations in calcination temperature is shown in **Figure 5**. The figure shows that the particle size distribution of TiO_2 is getting wider with increasing calcination temperature. TiO_2 nanoparticles without calcination are distributed in the 80 - 100 nm range with an average particle size of 99.41 nm (**Figure 5(a)**). At a calcination temperature of 200 °C, they were distributed in the 80 - 120 nm with an average particle size of 109.33 nm (**Figure 5(b)**). At the calcination temperature of 230 °C, they were distributed in the 150 - 225 nm range with an average particle size of 200.34 nm (**Figure 5(c)**). At the calcination temperature of 250 °C were distributed in the 150 - 400 nm with an average particle size is 269.45 nm (**Figure 5(d)**).

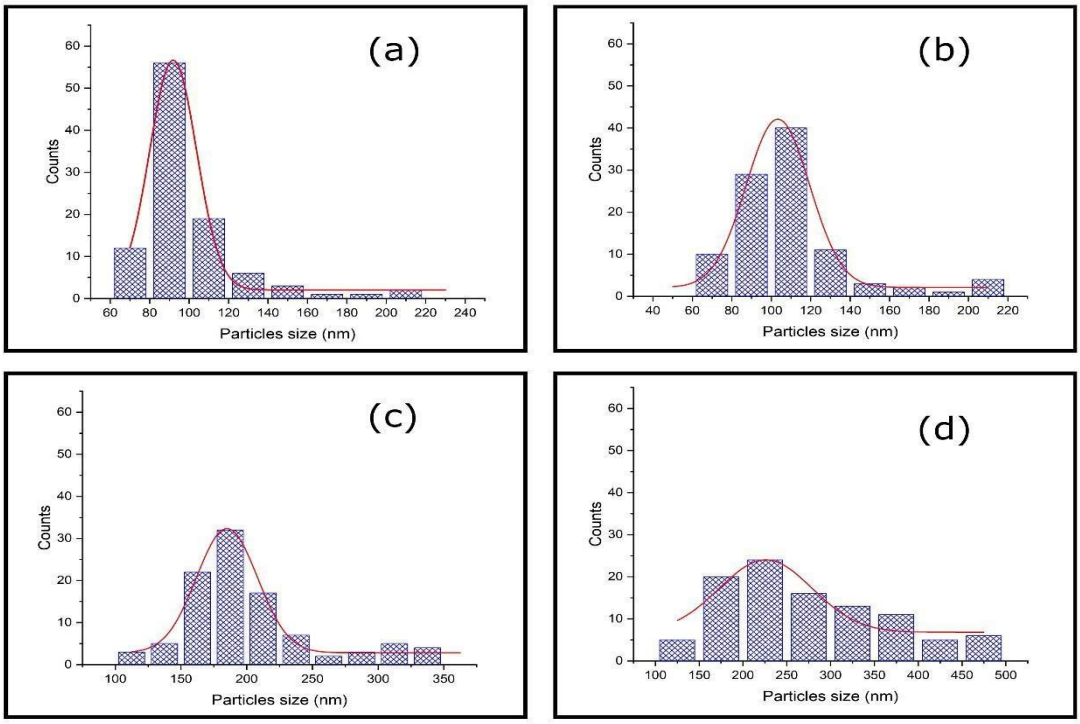

Figure 5 Particles size distribution of TiO_2 nanoparticles with variations in calcination temperature (a) uncalcined, (b) 200 °C, (c) 230 °C, and (d) 250 °C.

The impedance measurement results are shown in **Figure 6**. The 3 peak patterns are sharp, indicating that the TiO_2 nanoparticles that deposit QCM are rigid materials, so the material does not dissipate the QCM oscillation energy. The increase in calcination temperature agitates the agglomeration and the particle size. The expanded agglomeration and the enlargement of the particles resulted in the shift of the resonance frequencies series and parallel (f_s and f_p) to the lower side. The figure shows a change in the resonant frequency of the f_s series sequentially, namely 0.00050, 0.00108, 0.00123, and 0.00240 MHz.

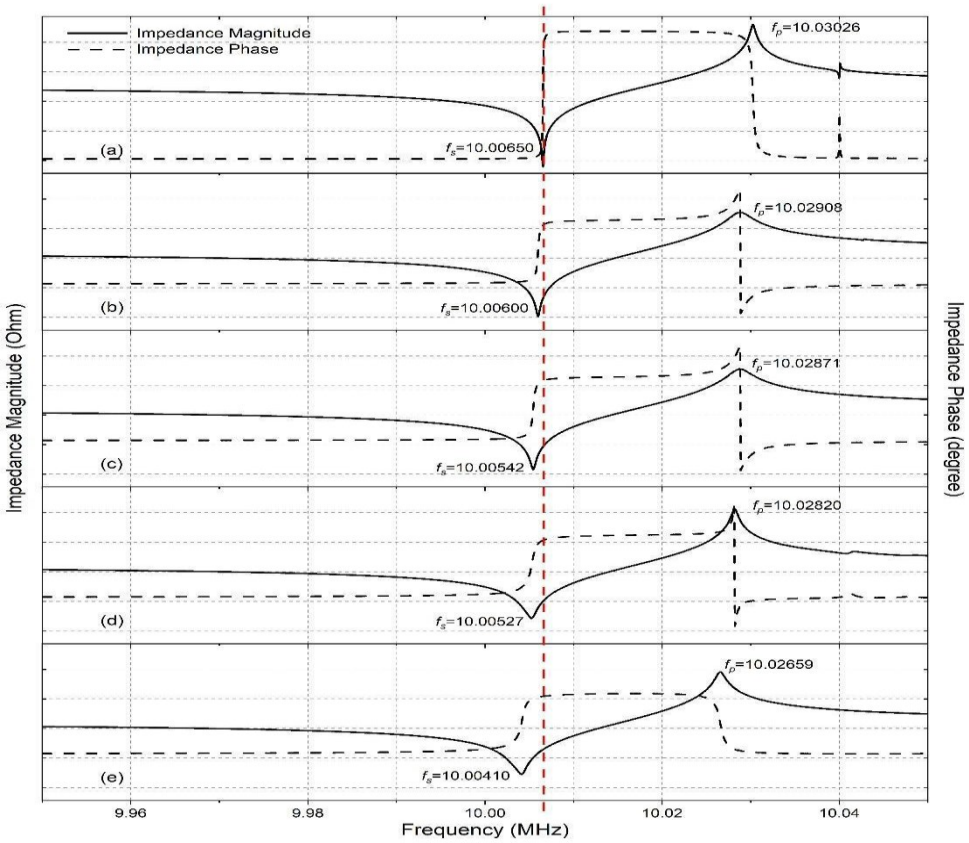

Figure 6 QCM impedance graphs that have been deposited with TiO_2 at different calcination temperatures (a) untreated, (b) uncalcined, (c) 200 °C, (d) 230 °C, (e) 250 °C.

Discussion

Calcination temperature in the ultrasonic spray pyrolysis method affects the TiO_2 nanostructure. The morphology and nanostructure of the deposited layer depend on the applied calcination temperature. The kinetic energy generated from the heating treatment will increase the kinetic energy of the particles. This energy is used to form nanoparticles [27]. The current results in (**Figure 4**) show that the increase of TiO_2 nanoparticles size and agglomeration occurs when the calcination temperature increases.

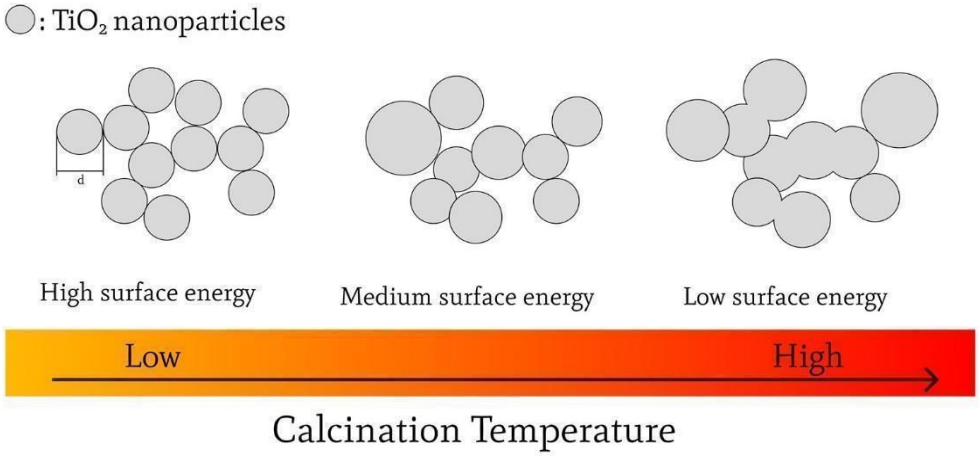

Figure 7 Illustration of increasing agglomeration with changes in calcination temperature.

The heat absorbed will provide energy in the process of growing TiO_2 particles. The higher the calcination temperature, the more energy is absorbed by the atoms so that the size of the particles increases; this is because the atoms have sufficient energy to pass through the particle grain boundaries. Based on the Ostwald Ripening Model, a mass transport phenomenon occurs due to surface diffusion between particles attached, so smaller particles will transfer their mass to become larger materials. Smaller size particles tend to have relatively large interfacial energies, which will donate their mass to larger particles [31]. As illustrated in **Figure 7**, when the temperature increases, the particle size will enlarge and tend to agglomerate. The energy received will bind the particles to 1 another, resulting in agglomeration [29]. The increase in particle agglomeration causes an increase in the mass deposited above the QCM, as shown in **Table 1**.

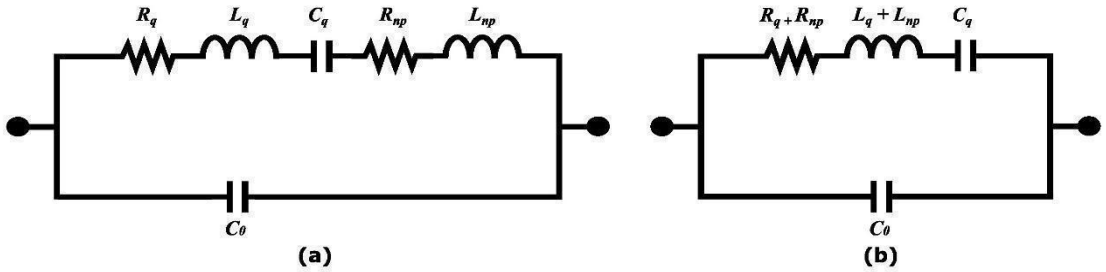

Figure 8 Butterworth-van Dyke circuit model of (a) coated with TiO_2 nanoparticles and (b) Simplified model of the BVD circuit.

The deposited TiO_2 nanostructure influences the impedance characteristics of the QCM. Based on a review of the BVD equivalent circuit, when QCM is added to the TiO_2 nanoparticle layer, the BVD circuit model is added with resistance (R_{np}) and inductance (L_{np}) factors in the R_q, L_q, and C_q series circuits (**Figure 8(a)**). The resonant frequency is determined from the impedance value (Z) expressed by Eq. (1);

$$Z = R + iX \tag{1}$$

where Z is the impedance value, R is the resistance which represents the energy dissipation, and X is the reactance which represents the energy stored in the BVD equivalent circuit. Based on the BVD equivalent circuit with the *RLC* series circuit, the impedance value in Eq. (1) can be reduced to Eq. (2);

$$Z = \sqrt{R^2 + (X_L - X_C)^2} \tag{2}$$

Or Eq. (3);

$$Z = \sqrt{R^2 + \left(\omega L - \frac{1}{\omega C}\right)^2} \tag{3}$$

QCM resonates when the X_L and X_C values have the same value. This makes the Z value minimum because the X_L - X_C value equals zero, so the Z value will be the same as the R-value. The BVD circuit model on the deposited QCM sensor (**Figure 8(a)**) is added with the Resistor factor (R_{np}) and Inductor (L_{np}) in the R_q, L_q, and C_q series circuits. **Figure 8(b)** simplifies the circuit model after the deposition of TiO_2 nanoparticles. So the series impedance value becomes [32,33];

$$Z_s = \sqrt{(R_q + R_{np})^2 + \left(\omega(L_q + L_{np}) - \frac{1}{\omega C_q}\right)^2} \tag{4}$$

because the circuit is in a resonant state, Eq. (4) can be expressed as follows;

$$Z_s = R_q + R_{np} \tag{5}$$

From Eq. (5), it can be concluded that the damping value of the TiO_2 nanoparticles will be equal to the Z_s value minus the damping value of the QCM sensor quartz. The results of the attenuation value of the TiO_2 nanoparticles were then plotted using the relationship between the calcination temperature and the Z_s and R_{np} values (**Figure 8**).

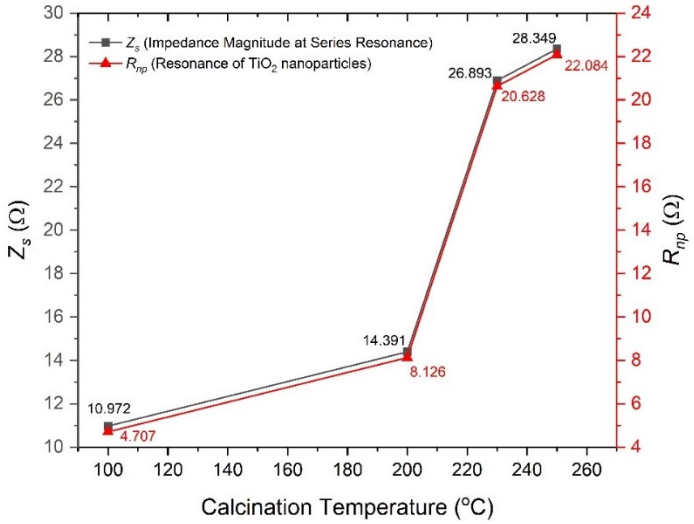

Figure 9 The relationship between the calcination temperature and the QCM damping and impedance.

Figure 9 shows that impedance and damping values also increase as the calcination temperature increases. The higher calcination temperature causes particle enlargement and agglomeration (**Figure 4**), increasing the QCM attenuation value. Based on **Table 1** shows the changes in frequency values for all variations that are applied have a value below 0.02001 MHz so that all layers are rigid layers. The layer is considered rigid if the value of the shift in the resonant frequency is not more than 2 % of the QCM resonant frequency (2 % of the resonant frequency = 0.02001 MHz) [34]. The value of the mass deposited above QCM can be determined using the Sauerbrey Eq. (6). Sauerbrey equation explains the relationship between changes in frequency (Δf) and mass of TiO_2 nanoparticles depositing QCM substrates (Δm) as shown in Eq. (6) [35];

$$\Delta m = -C \cdot \Delta f \tag{6}$$

C is the QCM constant, and Δf is the change in frequency [34,35]. The obtained mass of the deposited TiO_2 nanoparticles is presented in **Table 1**.

Table 1 Calculation of the mass and thickness of TiO_2 deposited on the QCM substrate based on the Sauerbrey equation.

T calcination (°C)	$f_s'(MHz)$	$\lvert\Delta f\rvert$ (MHz)	Δm (ng)
Uncalcined	10.00600	0.00050	4,333.12
200	10.00542	0.00108	9,359.53
230	10.00527	0.00123	10,659.50
250	10.00410	0.00240	20,799.00

The calculation results show that more and more TiO_2 nanoparticles are deposited on top of the QCM. The value of the frequency shift Δf in **Table 1** shows an increase. Based on calculations using Eq (1), the higher the frequency shift value Δf, the more mass Δm of TiO_2 nanoparticles deposited. The increase in the value of the resonant frequency shift indicates that the series and parallel resonant frequencies (f_s and f_p) of the QCM experience a lower shift as the calcination temperature increases (**Figure 6**). As previously discussed, the X_L and X_C values are the same when the resonator resonates. Thus, the resonant frequency equation can be obtained by substituting the value of ω with $2\pi f$.

$$X_L = X_C \tag{7}$$

$$2\pi fL = \frac{1}{2\pi fC} \tag{8}$$

and if Eq. (8) is simplified, then the *f* is obtained by;

$$f = \frac{1}{2\pi}\sqrt{\frac{1}{LC}} \tag{10}$$

by reviewing in **Figure 8(b)**, the *L* factor is the series result of the inductance value of quartz QCM L_q with the inductance of TiO_2 L_{np} nanoparticles, so Eq. (10) can be modified into Eq. (11) [32,36];

$$f = \frac{1}{2\pi}\sqrt{\frac{1}{(L_q+L_{np})C}} \tag{11}$$

Based on these parameters, the series frequency (f_s) value will change according to the L_{np} value of the layer mass inertial element. Meanwhile, the value of the parallel resonant frequency (f_p) is related to the capacitor resonance, paralleled between C_0 on the static arm and C_q on the motional arm [18].

It can be seen from **Figure 4** the higher calcination temperature stirs the particles to interdiffusion to produce larger and agglomerated particles. The agglomerates increase the mass of the TiO_2 nanoparticles according to the calculation results shown in **Table 1**. Increasing the mass of TiO_2 nanoparticles will increase the mass inertia (L_{np}) and will cause a shift in the value of the QCM series resonant frequency (f_s) to a lower direction. In addition, the damping value (R_{np}) will also increase and affect the impedance phase angle, which will be narrower. (**Figures 4(a) - 4(b)**) shows TiO_2 nanoparticles without calcination, and those calcined at 200 °C were spherical and separated with small sizes. Whereas in TiO_2 nanoparticles calcined at 230 °C (**Figure 4(c)**, the particles look bigger, and some particles diffuse. Based on the results of mass calculations, it shows that there is a mass change that is not large enough, so changes in mass inertia values (L_{np}) and damping (R_{np}) are not large enough either. When viewed from the impedance graph in (**Figures 6(b) - 6(d)**), the shift in the series resonant frequency (f_s) is decreasing but not large enough. Likewise, the impedance phase shown does not show a large change compared to the graph pattern The impedance of the uncoated QCM sensor shows that the damping effect of nanoparticles (R_{np}) does not significantly affect the impedance phase of the QCM sensor.

In contrast to the TiO_2 nanoparticles, which were calcined at 250 °C shown in **Figure 4(d)**, the particles seem to diffuse to each other to form agglomerates so that it has a high density of particles with a larger mass. The high density causes the addition of mass inertia (L_{np}), and damping (R_{np}) values are also greater. When viewed from the impedance graph in **Figure 6(e)**, it displays a shift in the series resonant frequency (f_s) with a large change in the impedance phase angle. The difference shows that the nanoparticles provide a sizeable damping effect (R_{np}), significantly affecting the sensor impedance and phase change.

Conclusions

Calcination temperature is essential in particle size and TiO_2 nanostructures. Due to the increased surface energy diffusion, particle agglomeration increases when the calcination temperature increases. As agglomeration and particle size increase, the impedance value and QCM frequency shift also increase. Furthermore, increasing the calcination temperature increased the diameter of the particles. Increasing the mass of TiO_2 nanoparticles will increase the mass inertia (L_{np}), causing a shift in the value of the QCM series resonant frequency (f_s) to a lower direction. In addition, the damping value (R_{np}) will also increase and affect the phase angle and impedance. Nanostructured TiO_2 particles deposited on the QCM substrate in this study obtained at 200 °C calcination temperature can be applied as a gas sensor.

Acknowledgments

The authors would like to thank KEMENRISTEKDIKTI through Lembaga Penelitian dan Pengabdian kepada Masyarakat (LPPM) Universitas Brawijaya (UB), Indonesia for being financially supported by Hibah Penelitian Dasar with contract no. 438/19/UN/10.C10/TU/2021. Thanks to the Laboratorium sentral ilmu hayati (LSIH) UB for assistance using the XRD dan SEM.

References

[1] ALD Silva, FJ Trindade, D Jean-Lou, B Ramos, SCTA Carlos and D Gouvêa. Synthesis of TiO_2 microspheres by ultrasonic spray pyrolysis and photocatalytic activity evaluation. *Ceram. Int.* 2022; **48**, 9739-45.

[2] M Ye, J Pan, Z Guo, X Liu and Y Chen. Effect of ball milling process on the photocatalytic performance of CdS/TiO_2composite. *J. Nanotechnology Rev.* 2020; **9**, 558-67.

[3] B Zhang, S Cao, M Du, X Ye, Y Wang and J Ye. Titanium dioxide (Tio_2) mesocrystals: Synthesis, growth mechanisms and photocatalytic properties. *Catalysts* 2019; **9**, 91.

[4] S Prasad, SS Kumar and VPM Shajudheen. Synthesis, characterization and study of photocatalytic activity of TiO_2 nanoparticles. *Mater. Today Proc.* 2020; **33**, 2286-8.

[5] S Cao, N Sui, P Zhang, T Zhou, J Tu and T Zhang. TiO_2 nanostructures with different crystal phases for sensitive acetone gas sensors. *J. Colloid Interface Sci.* 2022; **607**, 357-66.

[6] B Chen, P Li, B Wang and Y Wang. Flame-annealed porous TiO_2/CeO_2 nanosheets for enhenced CO gas sensors. *Appl. Surf. Sci.* 2022; **593**, 153418.

[7] HG Pozos, KTV Krishna, MDLLO Amador, Y Kudriavtsev and AM Alvarez. TiO_2 thin film based gas sensors for CO-detection. *J. Mater. Sci. Mater. Electron.* 2018; **29**, 15829-37.

[8] H Sun, T Lu-Qi, T Li, X Gao, T Sang, Y Li, Y Wei, G Wang, Z Peng, Y Gui, X Sheng-Yuan and J Li. TiO_2−Doped GeSe monolayer: A highly selective gas sensor for SF6 decomposed species detection based on DFT method. *Appl. Surf. Sci.* 2022; **572**, 151212.

[9] A Haider, G Ali, MJ Haider, MS Edan, R Al-Obaidy, A Thamir, MM Hathal, EM Abbas and F Al-Sheikh. Modification optical properties of TiO_2 nanostructure as solar cell. *Energ. Rep.* 2022; **8**, 77-85.

[10] VG Krishnan, A Purushothaman and P Elango. A study of the physical properties and gas-sensing performance of TiO_2 nanofilms: Automated nebulizer spray pyrolysis method (ANSP). *Phys. Status Solidi* 2017; **214**, 1700020.

[11] AM Laera, L Mirenghi, G Cassano, L Capodieci, MC Ferrara, S Mazzarelli, M Schioppa, D Dimaio, A Rizzo, M Penza and L Tapfer. Synthesis of nanocrystalline ZnS/TiO_2 films for enhanced NO_2 gas sensing. *Thin Solid Films* 2020; **709**, 138190.

[12] S Ji, H Esmaeilzadeh, J Su, S Pagsuyoin and H Sun. Novel analysis of a micropillar coupled acoustic wave sensor. *Sensor. Actuator. Rep.* 2021; **3**, 100034.

[13] M Procek, A Stolarczyk, T Pustelny and E Maciak. A study of a QCM sensor based on TiO_2 nanostructures for the detection of NO_2 and explosives vapours in air. *Sensors* 2015; **15**, 9563-81.

[14] Q Chen, S Xu, Q Liu, J Masliyah and Z Xu. QCM-D study of nanoparticle interactions. *Adv. Colloid Interface Sci.* 2015; **233**, 94-114.

[15] A Alassi, M Benammar and D Brett. Quartz crystal microbalance electronic interfacing systems: A review. *Sensors* 2017; **17**, 2799.

[16] NL Bragazzi, D Amicizia, D Panatto, D Tramalloni, I Valle and R Gasparini. Quartz-crystal microbalance (QCM) for public health: An overview of its applications. *Adv. Protein Chem. Struct. Biol.* 2015; **101**, 149-211.

[17] SP Sakti, DD Kamasi and NF Khusnah. Stearic acid coating material loading effect to quartz crystal microbalance sensor. *Mater. Today Proc.* 2019; **13**, 53-8.

[18] RJ Horst, A Katzourakis, BT Mei and SD Beer. Design and validation of a low-cost open-source impedance based quartz crystal microbalance for electrochemical research. *HardwareX* 2022; **12**, e00374.

[19] M Masruroh and DJDH Santjojo. The impedance analysis of a viscoelastic petalous structured stearic acid functional layer deposited on a QCM. *Sensors* 2022; **22**, 7504.

[20] R Aflaha, H Afiyanti, ZN Azizah, H Khoirudin, A Rianjanu, A Kusumaatmaja, R Roto and K Triyana. Improving ammonia sensing performance of quartz crystal microbalance (QCM) coated with nanofibers and polyaniline (PANi) overlay. *Biosens. Bioelectron. X* 2023; **13**, 100300.

[21] S Phromma, T Wutikhun, P Kasamechonchung, T Eksangsri and C Sapcharoenkun. Effect of calcination temperature on photocatalytic activity of synthesized TiO_2 nanoparticles via wet ball milling sol-gel method. *Appl. Sci.* 2020; **10**, 993.

[22] DP Dave and KV Chauhan. Synthesis of visible spectrum-active TiO_2 thin film induced by RF magnetron sputtering. *Mater. Today Proc.* 2022; **62**, 4254-9.

[23] B Dey, S Bulou, W Ravisy, N Gautier, M Richard-Plouet, A Granier and P Choquet. Low-temperature deposition of self-cleaning anatase TiO_2 coatings on polymer glazing via sequential continuous and pulsed PECVD. *Surf. Coating. Tech.* 2022; **436**, 128256.

[24] F Trabelsi, F Mercier, E Blanquet, A Crisci and R Salhi. Synthesis of upconversion TiO_2:Er3+-Yb3+ nanoparticles and deposition of thin films by spin coating technique. *Ceram. Int.* 2020; **46**, 28183-92.
[25] Wahyudiono, S Kawai, M Mardis, S Machmudah, H Kanda, Y Zhao and M Goto. Bimetallic nanoparticle generation from Au − TiO_2 film by pulsed laser ablation in an aqueous medium. *Alexandria Eng. J.* 2021; **60**, 2225-34.
[26] KS Shamala and M Vishwas. Influence of substrate temperature on optical, structural and dielectric properties of TiO_2 thin films prepared by spray pyrolysis technique. *Mater. Today Proc.* 2022; **52**, 1344-7.
[27] SR Ardekani, ASR Aghdam, M Nazari, A Bayat, E Yazdani and E Saievar-Iranizad. A comprehensive review on ultrasonic spray pyrolysis technique: Mechanism, main parameters and applications in condensed matter. *J. Anal. Appl. Pyrol.* 2019; **141**, 104631.
[28] P Majerič, D Jenko, B Friedrich and R Rudolf. Formation mechanisms for gold nanoparticles in a redesigned ultrasonic spray pyrolysis. *Adv. Powder Tech.* 2017; **28**, 876-83.
[29] J Banjuraizah, YP Ong and ZA Ahmad. Effect of calcination temperature on titanium dioxide synthesized by Sol-Gel method. *Int. J. Curr. Res. Sci. Eng. Tech.* 2018; **1**, 68.
[30] R Rudolf, Ž Jelen, S Stopić and IP Majerič. Ultrazvočna razpršilna piroliza materialov, na primeru TiO_2 nanodelcev. *Anali PAZU* 2022; **11**, 52-63.
[31] L González-Reyes, I Hernández-Pérez, LA Díaz-Barriga, H Dorantes-Rosales, E Arce-Estrada, R Suárez-Parra and JJ Cruz-Rivera. Temperature effects during Ostwald ripening on structural and bandgap properties of TiO_2 nanoparticles prepared by sonochemical synthesis. *Mater. Sci. Eng. B* 2010; **175**, 9-13. 2010,
[32] M Abdul and A Qabazard. Resonance circuits and applications. *Int. J. Inventive Eng. Sci.* 2015; **3**, 6-13.
[33] DAP Wardani, B Hariyanto, N Kurniawati, NP Har, N Darmawan and Irzaman. Synthesis of silicon dioxide (SiO_2) from reeds biomass (Imperata cylindrica) and the analysis of electrical properties (study cases: Impedance, resistance, capacitive reactance, inductive reactance). *J. Phys. Conf. Ser.* 2021; **2019**, 012064.
[34] X Qiao, X Zhang, Y Tian and Y Meng. Progresses on the theory and application of quartz crystal microbalance. *Appl. Phys. Rev.* 2016; **3**, 031106.
[35] G Sauerbrey. Verwendung von Schwingquarzen zur Wägung dünner Schichten und zur Mikrowägung. *Zeitschrift für Physik* 1959; **155**, 206-22.
[36] I Burda. Quartz crystal microbalance with impedance analysis based on virtual instruments: Experimental study. *Sensors* 2022; **22**, 1506.